RESEARCH PAPER

Experimental investigation of the face stability of shallow tunnels in sand

Ansgar Kirsch

Abstract Various models have been proposed for the prediction of the necessary support pressure at the face of a shallow tunnel. To assess their quality, the collapse of a tunnel face was modelled with small-scale model tests at single gravity. The development of the failure mechanism and the support force at the face in dry sand were investigated. The observed displacement patterns show a negligible influence of overburden on the extent and evolution of the failure zone. The latter is significantly influenced, though, by the initial density of the sand: in dense sand a chimney-wedge-type collapse mechanism developed, which propagated towards the soil surface. Initially, loose sand did not show any discrete collapse mechanism. The necessary support force was neither influenced by the overburden nor the initial density. A comparison with quantitative predictions by several theoretical models showed that the measured necessary support pressure is overestimated by most of the models. Those by Vermeer/Ruse and Léca/Dormieux showed the best agreement to the measurements.

Keywords Face stability · Shallow tunnels

A. Kirsch (✉)
Division of Geotechnical and Tunnel Engineering,
University of Innsbruck, Technikerstr. 13,
6020 Innsbruck, Austria
e-mail: ansgar.kirsch@gmx.de

Present Address:
A. Kirsch
ILF Consulting Engineers, Feldkreuzstr. 3,
6063 Rum/Innsbruck, Austria

1 Introduction

The face stability of shallow tunnels must be guaranteed to minimise settlements at the ground surface and to prevent collapse of the soil ahead of the tunnel. For slurry and EPB shield machines, a *necessary support pressure*, p_f, must be prescribed to counteract water and earth pressure with a sufficient safety margin. While the water pressure can be predicted well, the determination of the resultant earth pressure on the face is rather vague. This becomes manifest in the relatively high partial safety factors on the earth pressure (e.g. STUVA [50], ZTV-Ing. [7]). In spite of all progress in research and technology, face collapses during construction of shallow tunnels still occur [47] and lead to significant construction delays and remediation costs.

For the determination of the necessary support pressure theoretical models as well as laboratory tests and numerical calculations have been published.

The theoretical approaches can be subdivided into kinematic approaches with failure mechanisms (e.g. Horn [23] and variations [2, 3, 13, 21, 37], Vermeer et al. [58], Krause [31], Léca and Dormieux [34] and derivations [44, 45, 46]) and static approaches with admissible stress fields (e.g. Léca and Dormieux [34], Atkinson and Potts [4]). Some additional approaches are neither purely kinematic nor purely static (Kolymbas [29], Balthaus [5]).

The experimental investigations of face stability range from experiments at single gravity, so-called *1g model tests* (e.g. Takano et al. [52], Sterpi and Cividini [48]) to *centrifuge tests* at multiples of g (e.g. Chambon and Corté [8, 9], Al Hallak et al. [1], Plekkenpol et al. [42], Kamata and Mashimo [25], Kimura and Mair [26]).

Among others, Ruse and Vermeer [43, 57, 59] investigated the necessary support pressure for the face of shallow tunnels with finite elements, making use of a linear elastic,

perfectly plastic constitutive model with a Mohr–Coulomb failure condition for the soil. From their numerical results, Ruse and Vermeer derived an empirical equation for the determination of p_f.

A comparison of some selected models was made by a simple example calculation (cf. Kirsch and Kolymbas [27, 28]). The dimensionless factor $N_D = p_f/(\gamma D)$ was calculated for a shallow circular tunnel with a diameter $D = 10$ m and an overburden $C = 10$ m (cf. Fig. 1). The soil properties were self-weight $\gamma = 18$ kN/m³ and cohesion $c = 0$, the friction angle was varied. No surcharge on the ground surface and no groundwater were considered.

The following models were compared:

- Horn model (theoretical, upper bound),
- Krause (theoretical, upper bound),
- Léca/Dormieux (theoretical, upper bound),
- Kolymbas (theoretical),
- Ruse/Vermeer (empirical, from FE calculations).

The predictions (Fig. 2) showed a large amount of scatter: for a given friction angle of, say, $\varphi = 32°$, the model responses vary between $N_D \approx 0$ and $N_D \approx 0.23$. Thus, the choice of *the* appropriate model for calculation of the necessary support pressure is not easy. Some models predict support pressures that might be too high. This could lead, in an extreme case, to blow-outs or heave at the ground surface (as reported by Holzhäuser et al. [22]). With other models the calculated support pressure might be too low, and the tunnel face could collapse.

Tunnelling, in general, is characterised by a complex interaction between support and ground. Current research interest is mainly focussed on numerical analysis (e.g. [18, 20, 24, 32, 36]). But the validity of numerical analyses needs to be checked either by in situ measurements or by laboratory model tests. To further assess the quality of proposed models for face stability analysis, the author performed two series of small-scale model experiments, which are described in the following. In the first series of experiments, the evolution of failure mechanisms in dense and loose sand with different overburden was investigated,
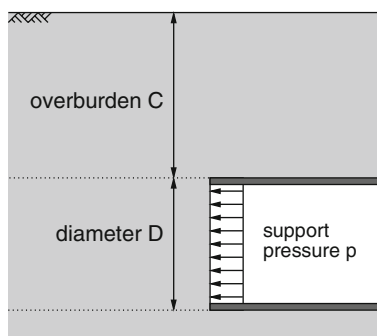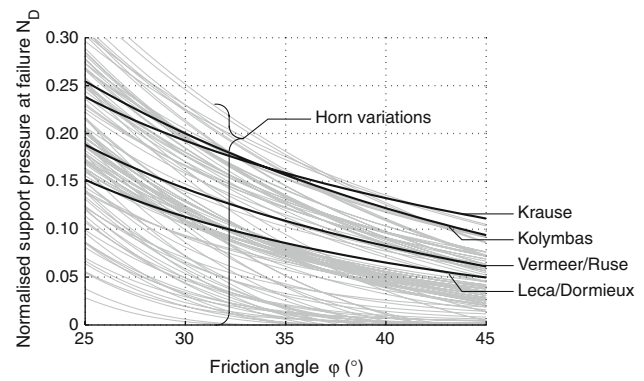

Fig. 1 Tunnel geometry

Fig. 2 Relation between N_D and φ for different models, $C/D = 1.0$

making use of Particle Image Velocimetry. The resulting support force on the tunnel face was studied in a second series of experiments. A comparison of the author's experimental results with predictions by several theoretical/numerical models concludes the paper.

2 Investigation of failure mechanisms

2.1 Size effects for small-scale model tests

When resorting to small-scale models, special attention must be drawn to scaling laws and size effects. Physical modelling can only reveal meaningful interpretations, when the measured quantities in the model are *similar* to quantities on the prototype scale. Basic requirements for the transfer of results from one scale to the other are formulated as scaling laws (cf. [14, 39]).

2.1.1 Similarity and deterministic size effect

The Π-*theorem* can be used to relate results from model and prototype. It states that i governing quantities of a physical problem, x_i, can be expressed in terms of j dimensionless variables, Π_j, which are products of different powers of the x_i. Thus, any functional relation between the physical quantities can be transferred to a relation of dimensionless products (cf. [14, 30]). Functional relations between the dimensionless products hold on different scales, if

$$\Pi_{j,\text{model}} = \Pi_{j,\text{prototype}}. \tag{1}$$

True similarity is only given if *all* determining properties are scaled correctly with respect to the fundamental dimensions. If not all properties are scaled consistently, similarity is only partly fulfilled and it remains engineering judgement to decide whether this has a significant influence on the results or not. For these similarity requirements, it is very difficult to model

cohesive soils with 1g model tests. Therefore, the author decided to perform all tests with dry sand.

Especially for geotechnical problems, the deterministic size effect (also called scaling effect) needs to be considered. In small-scale model tests, usually the geometry of the prototype structure is scaled down. But in most cases, the tested material is *not* scaled according to the scaling rules, which is referred to as *scaling effect*. It is, on the contrary, common practice to use the prototype sand (with a mean grain diameter d_{50}) for the model as well. Thus,

$$\left(\frac{d_{50}}{D}\right)_{\text{model}} \neq \left(\frac{d_{50}}{D}\right)_{\text{prototype}}. \tag{2}$$

In this case, modelling errors can be expected when shear bands form and dilation of the material leads to restraints in the soil body (e.g. [15, 61, 60, 54]). Dilation effects in the model can be largely overestimated with respect to the prototype. Also the relation between mean grain diameter d_{50} and width of the shear band d_s plays a role: Nübel [40] found values for d_s/d_{50} between 10 and 20. It is generally assumed that d_s depends on relative density I_d [16].

Considering the above-mentioned statements, for the same material with the same density index, the width of a shear band in the model and in the prototype would be roughly the same. Thus, the Π -relation (2) can be paraphrased to:

$$\left(\frac{d_s}{D}\right)_{\text{model}} \neq \left(\frac{d_s}{D}\right)_{\text{prototype}}. \tag{3}$$

If shear bands do not govern the system behaviour, some measures can be taken to minimise the scaling effect: the Technical Committee TC2 (Physical Modelling in Geotechnics) of the ISSMGE put together a catalogue of scaling laws and similitude questions in centrifuge modelling [54]: to minimise grain size effects on soil–structure interaction of a tunnel face stability problem, the following relation is recommended (cf. also Chambon et al. [10]):

$$\frac{D}{d_{50}} > 175. \tag{4}$$

In the performed experiments, two model sands (Table 1) were investigated, a sand *S1* with a mean diameter $d_{50} = 0.58$ mm ($\leadsto D/d_{50} \approx 170$) and a fine sand *S2* with $d_{50} = 0.24$ mm ($\leadsto D/d_{50} \approx 420$). Thus, (4) was more or less fulfilled.

In addition, Muir Wood [39] underlined the importance of taking soil nonlinearity into account: even if a set of dimensionless variables is found that characterises the given problem, it must be thoroughly investigated if these variables are really scale-independent: to give an example, the friction angle φ can be considered a dimensionless

Table 1 Properties of the applied sand, cf. [33]

Property		Sand (*S1*)	Fine sand (*S2*)
Mean grain size	d_{50}	0.58 mm	0.24 mm
Coefficient of uniformity	U	3.6	1.9
Grain shape		Angular to subangular	
Max. void ratio	$e_{\max}$	0.75	0.87
Min. void ratio	$e_{\min}$	0.42	0.56
Critical state friction angle	φ_c	32.5°	31.3°

parameter in physical modelling of soils; the Π-theorem states that $\varphi_{\text{model}} = \varphi_{\text{prototype}}$, which does not hold generally for dense sand. Also the soil stiffness needs to be treated with care, if the displacements of the soil body are of primary concern.

2.1.2 Stochastic size effect

Also a stochastic size effect must be taken into account when transferring results from model to prototype scale. It has, for example, been shown that the shear resistance in non-cohesive soils decreases with increasing size of the sample [53, 55]. The stochastic size effect is due to the random distribution of material properties, such as void ratio, grain sizes or local strength. The macroscopic strength of a soil sample reduces with increasing size because the number of weak spots increases.

Unfortunately, experimental investigations of above-mentioned effects in sand are rare. Therefore, there have been efforts to investigate the stochastic size effect numerically. E.g. Tejchman and Górski [56] resorted to numerical simulations of shear localisation in plane strain shearing of an infinite granular layer. To capture the essential features of shear localisation realistically, the authors made use of a mico-polar hypoplastic model. Their results show that the deterministic size effect is rather small, at least in terms of mobilised friction angle. The results for a random distribution of initial void ratio indicate a reduction in peak shear strength with increasing specimen size, but no significant influence on residual strength.

Above remarks should be kept in mind when looking at the results of both test series. Further reference to the size effects will be made where necessary.

2.2 Experimental set-up and tested materials

2.2.1 Sandbox and tunnel model

The first series of experiments was conducted in a model box (Figs. 3, 4) with inner dimensions 37.2 × 28.0 × 41.0 (width × depth × height in cm). The outer frame was made of steel, bottom and side walls wooden, and the front
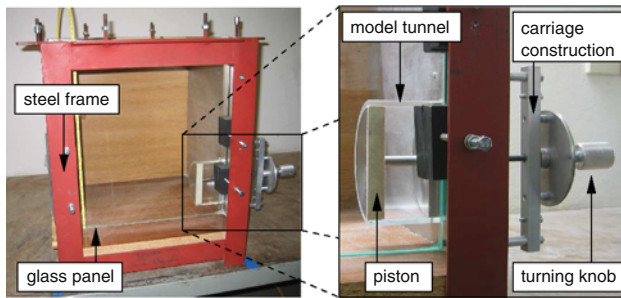
Fig. 3 Box and model tunnel for the first series of experiments

wall was 1-cm thick hardened glass. The soil grains adjacent to the glass wall could be observed throughout the test.

The problem was modelled in half, cutting through the tunnel axis vertically. Therefore, the tunnel was represented by a half-cylinder of perspex, with an inner diameter of 10.0 cm and a wall thickness of 0.4 cm. This model tunnel protruded 7.0 cm into the soil domain. An aluminium piston was fitted into the tunnel to support the soil.

The piston was mounted on a horizontal steel rod, and its perimeter was covered with a felt lining. The felt lining prevented sand grains from entering the gap between piston and glass wall. In the first series of experiments, no forces were measured; therefore, it was not considered necessary to reduce the friction between piston and tunnel wall.

To trigger collapse of the face, the piston could be retracted into the model tunnel by turning a knob in extension of the piston axis (Fig. 3, right). One revolution of the knob led to 1-mm horizontal displacement.

2.2.2 Sand properties

Commercially available quartz sand with two different grain size distributions was used: a sand with grain diameters between 0.1 and 2.0 mm (*S1*) and a fine sand with grain sizes

between 0.1 and 0.5 mm (*S2*); some properties are listed in Table 1.

2.3 Test procedure

2.3.1 Preparation of the sand body

The tests were performed with dry sand for various *C/D* ratios and different initial densities I_d,

$$I_d \approx \frac{e_{\max} - e}{e_{\max} - e_{\min}}, \tag{5}$$

$e_{\max}$ and $e_{\min}$ being the maximum and minimum void ratios determined from standardised density index tests (e.g. DIN 18126 [12]).

The *dense* samples were prepared by dry pluviation of sand into the box with a funnel. With a drop height of 10 cm, layers of 5 cm thickness were installed. These layers were then compacted manually by hand tamping with approximately the same compaction energy for each layer. The *loose* samples were prepared by carefully putting the sand into the box with a small shovel, trying to prevent any compacting action.

The quoted void ratios e and resulting densities I_d must be understood as average values throughout the whole sample. For each test, an average void ratio e was calculated as

$$e = \frac{\rho_s}{m_d / V} - 1,$$

with the mass of the sand inside the box m_d and the occupied volume V.

2.3.2 Steps of the model tests

In the course of the experiment, the piston was retracted into the model tunnel, which triggered the face collapse. In
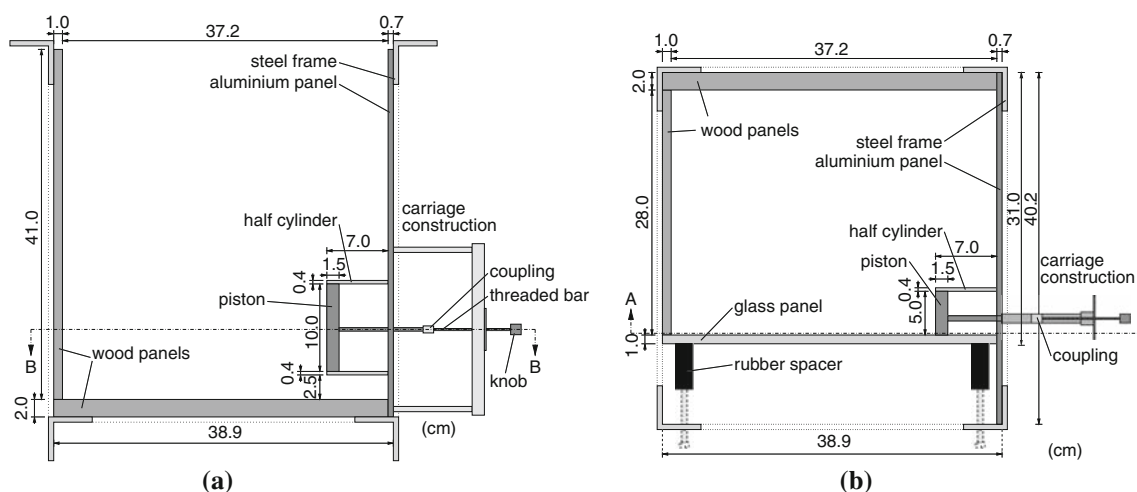

Fig. 4 Schematic sketch of the box for the first series of experiments. **a** Longitudinal section A-A. **b** Plan section B-B

doing so, the soil *displacements* at the tunnel face were prescribed, not the (support) *pressure*. This was, admittedly, not in agreement with the real problem, where the *pressure* inside the slurry is adjusted. Other researchers [8, 38] used inflatable membranes to support the soil. But as it is not possible to capture strain softening effects of the material in a stress-controlled test, the author decided to prescribe the displacements of the soil in front of the face, a solution also adopted by e.g. Kamata and Mashimo [25].

For the first 6.0 mm of piston displacement, increments $\Delta s = 0.25$ mm were chosen. This increment size corresponds to $0.5 \, d_{50,S1}$ and $1.0 \, d_{50,S2}$ and was considered small enough to capture the soil deformation at the onset of failure with sufficient accuracy. For another 19 mm, Δs was 0.5 mm, leading to an overall displacement of 25 mm. After each increment, a digital picture of the grain structure was taken.

2.4 Evaluation of soil displacements with Particle Image Velocimetry

The model tests of the first series were evaluated with Particle Image Velocimetry (PIV). PIV is a non-invasive technique that allows quantitative investigation of plane displacement patterns. In the last years, it has been increasingly applied to geotechnical applications because it allows to investigate the displacement fields in a soil sample on a grain-scale level (e.g. Nübel [40, 41], White et al. [62, 63], Mähr [35], Hauser [17]). Input for the PIV analysis were high-resolution pictures of consecutive (displacement) states of the grain skeleton.

2.4.1 Equipment and set-up

Figure 5 shows the set-up of the experiment with sandbox, camera and spotlight. The experiments were executed in a
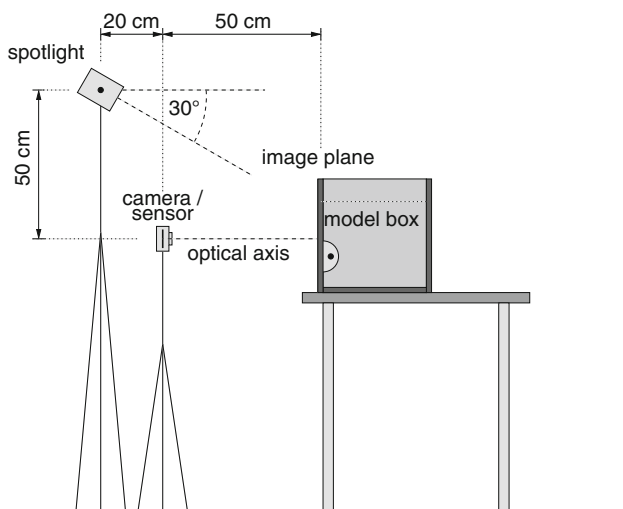

Fig. 5 Set-up of the tests

laboratory room without daylight. The spotlight was the only source of light, supplying a constant illumination of the box throughout a test. In order to create a diffuse lighting regime, a white sheet of paper was fixed on the spotlight. To avoid any reflection of the light source on the resulting pictures, the spotlight was positioned 50 cm above the camera, with an approximate inclination of 30° versus the horizontal (Fig. 5). Pictures were taken with a digital camera *Minolta Dimage 7i* with a maximum resolution of 5 Megapixels (2,560 px × 1,920 px). The resolution of the pictures in terms of mean grain diameters was $0.25 \, d_{50,S1}$/px for material *S1* and $0.6 \, d_{50,S2}$/px for material *S2*.

2.4.2 Postprocessing the pictures

In the present study, only quasi-static deformations were regarded; inertia was not considered a governing model parameter, and the behaviour of dry sand was assumed to be rate-independent. The digital pictures were post-processed by the free PIV package MatPIV v. 1.6.1 by Sveen [51].

The basic idea of PIV is image correlation of *interrogation cells* in consecutive pictures. These interrogation cells cover a few sand grains and are characterised by a certain pattern of light and shadow in the grain assembly. Primary results of a PIV evaluation are fields of incremental displacements $\mathbf{u}(\mathbf{x}, \Delta t_i)$ between subsequent pictures $i - 1$ and i. The results represent an *Eulerian* description of the movement, because the software uses a fixed reference coordinate system for all steps. This was appropriate for the purpose of this study, because the vector fields of incremental displacements can be interpreted as velocity fields. These were used for the detection of failure mechanisms.

2.4.3 Visualisation of results

The fields of incremental displacements can be visualised with *arrows* (Fig. 6a). For illustration purposes, in Fig. 6 and subsequent figures the tunnel lining and the piston contour are highlighted. Thus, the *directions* of the displacements are well recognisable. Figure 6 b shows a *colour* plot: different lengths of the displacement vectors are represented by different colours (online version) resp. levels of grey (print version). In this mode of visualisation, it can easily be seen which parts of the soil body move and which not. However, the information about the direction of the movement is lost.

A "mesh study" served to determine the optimum size of the interrogation cells. As a result, the author decided to perform the main investigation for material *S1* with a minimum cell size of 16 × 16 px. This size combines a sufficient quality with a good resolution. Moreover, the edge length corresponds to $4 \, d_{50,S1}$, which is smaller than
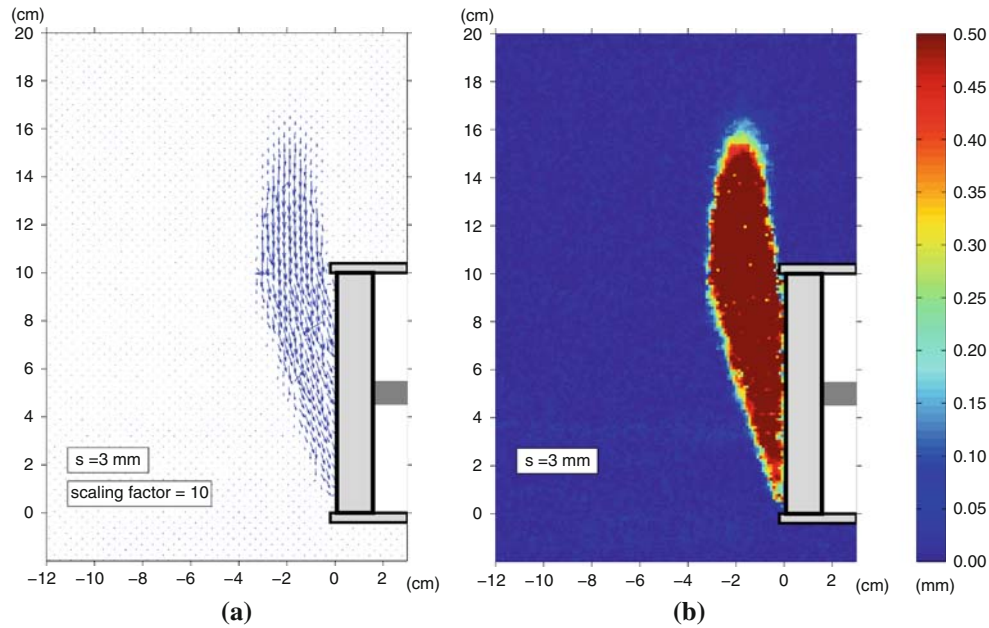
Fig. 6 Visualisation of incremental displacements for a piston advance from 2.25 to 2.50 mm (dense sand, $C/D = 1.0$). **a** Vector plot. **b** Colour plot

the expected width of shear bands (in the order of 10–20 times $d_{50,S1}$ for initially dense samples). For material *S2*, the best results were obtained with a cell size of 24 × 24 px.

2.4.4 Further processing of the information

With the following assumptions, the incremental displacement fields were further processed:

- the soil can be treated as a continuum,
- small strains per increment,
- plane strain conditions in the axis of symmetry.

Incremental strains $\boldsymbol{\varepsilon}$ were derived from incremental displacements $\mathbf{u}$ in distinct grid points (Fig. 7) making use of a two-dimensional finite difference scheme.

From the strain field, e.g. incremental volumetric strains

$$I_1^\varepsilon = \text{tr } \boldsymbol{\varepsilon} = \varepsilon_{11} + \varepsilon_{22} = \varepsilon_{\text{vol}} \tag{6}$$

and incremental shear strains

$$I_2^\varepsilon = \sqrt{\text{tr}(\boldsymbol{\varepsilon}^{*2})} = \sqrt{\varepsilon_{ij}^* \varepsilon_{ij}^*}, \tag{7}$$

with

$$\boldsymbol{\varepsilon}^* = \boldsymbol{\varepsilon} - 1/2 \text{tr} \boldsymbol{\varepsilon} \mathbf{1},$$

can be assessed.

The curl of the incremental displacements field

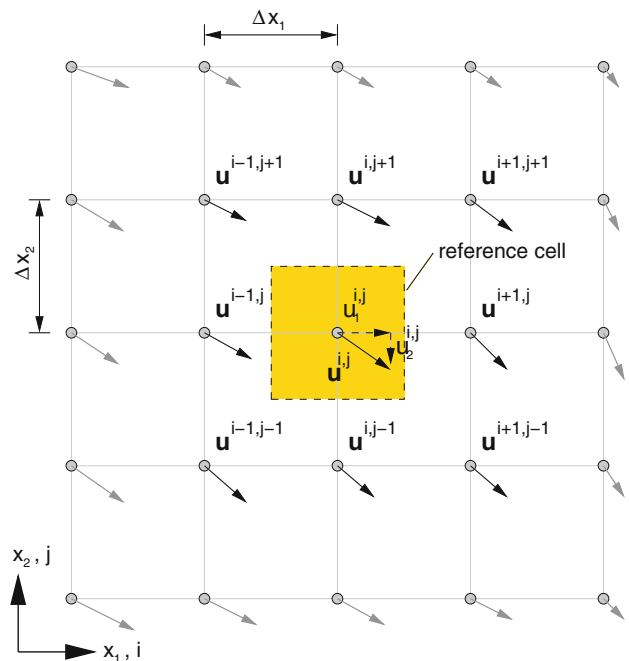$$\text{curl } \mathbf{u} = \frac{\partial u_1}{\partial x_2} - \frac{\partial u_2}{\partial x_1}, \tag{8}$$

Fig. 7 Grid of incremental displacement vectors $\mathbf{u}$

is a measure of (microscopic) circulation around the out-of-plane axis in every point and helps to visualise the failure process. It should not be confused with the rotation of particles, which cannot be evaluated with the applied PIV technique.

2.4.5 Limitations of PIV for the given problem

The investigated problem is a three-dimensional one. Obviously, evaluation of pictures of one problem boundary does not reveal the out-of-plane deformation. Nevertheless, expected out-of-plane movements were minimised by observing soil movements in the axis of symmetry.

Also, friction between sand and glass panel influences the mobility of the sand grains and may, thus, cause a deviation of the observed from the true collapse pattern. This influence was neglected because the focus of the evaluation was not on the *absolute* displacements of the sand grains. More specifically, the directions of movement and relative displacements were important. The author assumes that relative displacements are approximately the same for experiments with and without friction between sand and glass.

2.5 Results

The description of PIV results will focus on experiments with material *S1*. If not stated otherwise, the experiments with material *S2* revealed the same qualitative soil behaviour. An investigation of the scaling effect by comparing materials *S1* and *S2* follows in Sect. 2.6.

2.5.1 Incremental displacements

Figure 8 shows colour plots of incremental displacements for an advance step from 1.00 to 1.25 mm for different cover-to-diameter ratios and relative densities. The shape and extent of the failure zone did *not* depend on the height of the cover, because the pictures are virtually identical for different *C/D* values.

The influence of the soil density was much more pronounced: while the dense samples showed a clearly defined failure zone, this zone was rather diffuse for the loose samples. Moreover, soil movements reached up to the ground surface for the loose samples; whereas for the dense ones, movements were concentrated in the vicinity of the tunnel face.

2.5.2 Development of the failure zone with advancing piston

For the dense samples, a propagation of the failure zone was observed. This zone started from a wedge-like structure in front of the piston and subsequently extended vertically upwards. On the contrary, for the loose sand, no distinct development of the failure zone could be detected.

As mentioned earlier the incremental displacements are the primary result of the PIV evaluation. Other quantities such as volumetric and shear strains and curl were derived from the displacement field. The differentiation of the displacement field leads to an increase in "noise" of the derived quantities. Therefore, the author concentrated on qualitative interpretations of the results.

2.5.3 Incremental volumetric strains

Figure 9 shows a plot of incremental volumetric strains I_1^ε for different advance steps. It becomes clear, how the initially dense sample (top row of Fig. 9) changed its density ahead of the face. The red (resp. light grey) areas in the crown of the arch show how the sand loosened in a well-defined chimney towards the soil surface. In an initially loose soil (bottom row of Fig. 9), the soil loosened further in parts of the soil domain, in others it densified.

2.5.4 Incremental shear strains

Figure 10 shows the incremental shear strains I_2^ε for dense and loose samples at various steps of piston advance. The dense samples showed a well-defined concentration of shear strains (dark lines). The concentration zones form an arch ahead of the tunnel. Single features extend like "branches" above the arch.

For the loose samples, shear strains were distributed in rather large shear *zones*, which also show some minor shear strain concentrations, though.

2.5.5 Curl of the displacement field

In plots of the curl (Fig. 11), the red colour (resp. light grey) indicates a counter-clockwise, the blue colour (resp. dark grey) a clockwise circulation of the vector field. For the dense samples, a concentration of circulation in well-defined zones can be observed. A circulation band indicating clockwise circulation starts from the bottom of the tunnel and heads towards the surface. A corresponding band with counter-clockwise circulation heads from the tunnel crown upwards. The two bands touch above an arch that is formed ahead of the tunnel.

The loose samples show a tree-like pattern of circulation that extends into the soil domain in motion and does not change with increasing piston displacement.

2.6 Interpretation of results

2.6.1 Dense sand

The shape and extent of the observed failure zone is in good qualitative agreement with centrifuge experiments by Chambon and Corté [8], Kamata and Mashimo [25] and 1g model tests by Takano et al. [52].
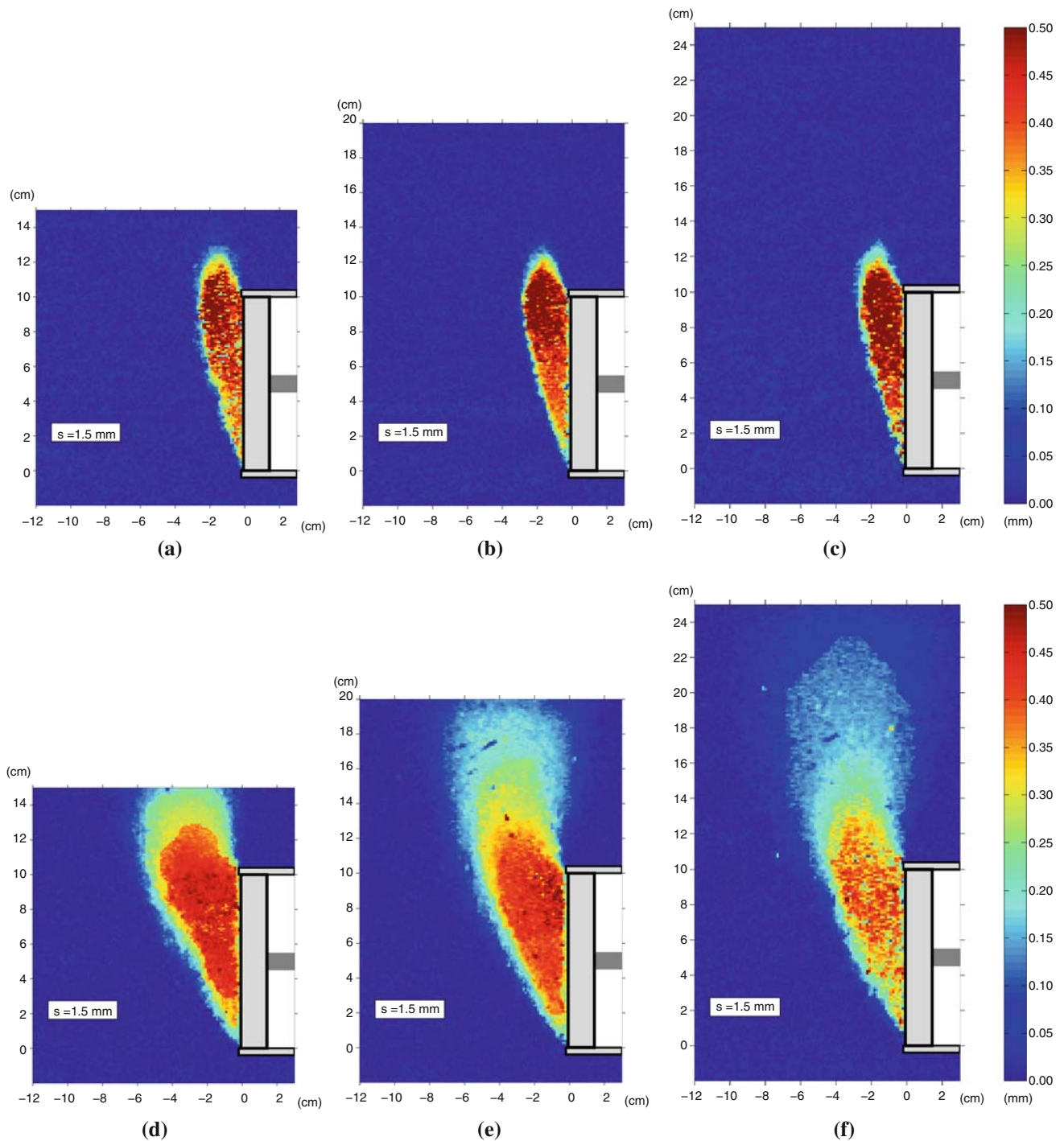
Fig. 8 Incremental displacements for a piston advance from 1.00 to 1.25 mm for different C/D and I_d values with material $S1$; *top row*: dense samples ($I_d = 0.80 \ldots 0.85$), *bottom row*: loose samples ($I_d = 0.26 \ldots 0.29$). **a** Dense, $C/D = 0.5$. **b** Dense, $C/D = 1.0$. **c** Dense, $C/D = 1.5$. **d** Loose, $C/D = 0.5$. **e** Loose, $C/D = 1.0$. **f** Loose, $C/D = 1.5$

The PIV analyses show that the overburden had a negligible influence on the shape and extent of the failure zone for dense soil samples. The impact of density was much more pronounced: in dense sand the failure zone developed stepwise towards the ground surface. As soon as it reached

the ground surface, a chimney-like and a wedge-like part could be distinguished (Fig. 12). This configuration resembles the theoretical Horn model.

There is one important restriction, though: no intermediate shear bands were detected at the crown level of the model
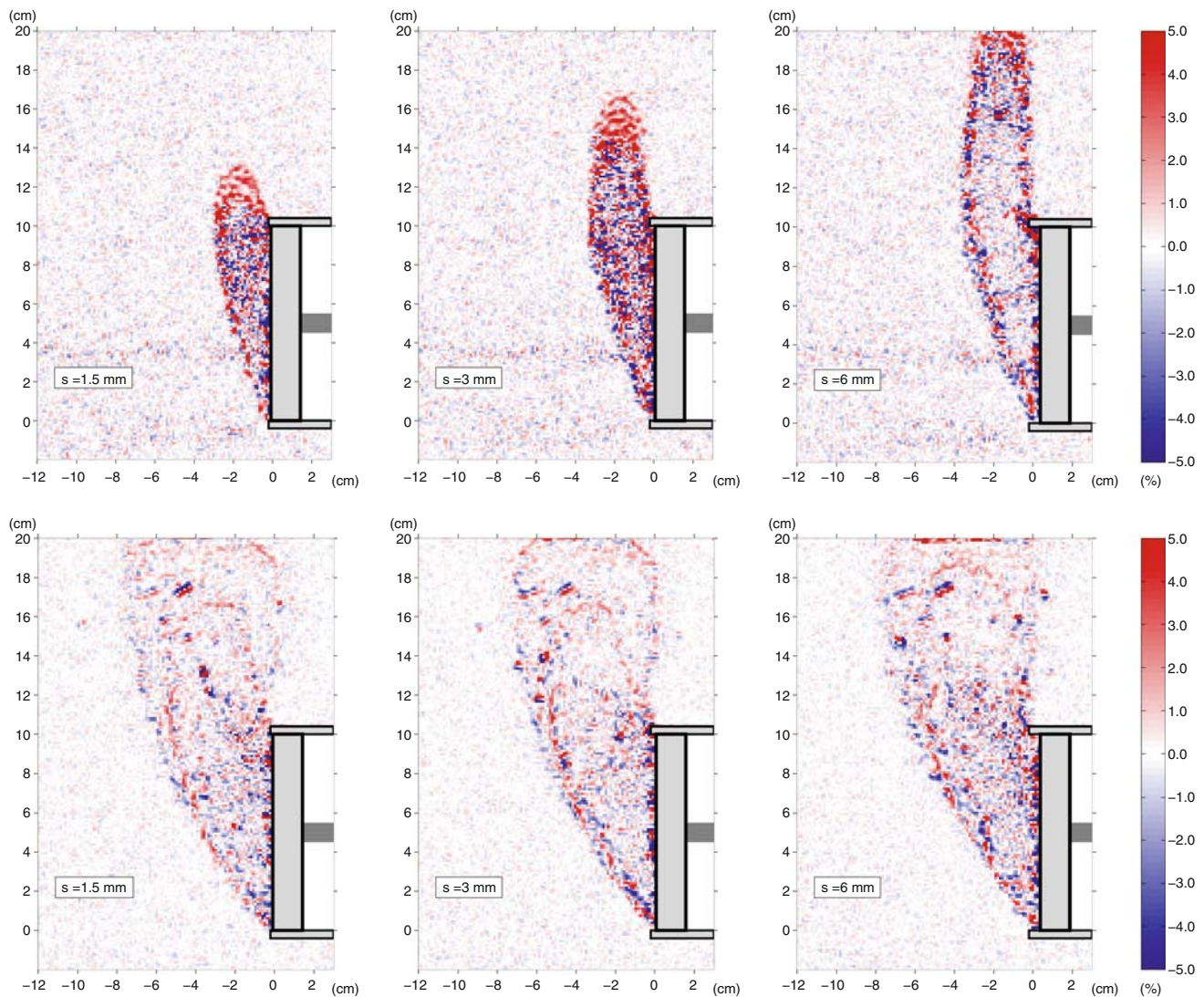
Fig. 9 Incremental volumetric strains I_1^ε for different advance steps and different relative densities in material *S1*; *top row*: dense sample ($I_d = 0.83$), *bottom row*: loose sample ($I_d = 0.26$)

tunnel. The observations rather indicate a zone between chimney and wedge, in which the incremental displacement vectors continuously changed their orientation.

Therefore, Horn's assumption of a *rigid-block* mechanism is not supported by the author's experiments. But it is an open question whether the energy dissipated in the observed shear zone is more or less equal to that dissipated in a discrete shear plane.

2.6.2 Loose sand

For the loose samples, the PIV evaluations reveal a rather diffuse failure zone, which did not significantly change its shape throughout the test. Some shear "features" can be detected, reaching from the crown and invert of the model tunnel to the soil surface. The intensity of shearing is clearly

not as high as in the initially dense samples. The shape of the failure zone does not resemble any of the proposed models, described in the literature.

2.6.3 Shear band width

For the sake of comparison to other investigations, the width of the shear bands, d_s, as a multiple of the mean grain diameter d_{50} was also examined. Plotting the I_2^ε-values across a shear band, d_s was taken as the width of the resulting curve at approx. 50% of the peak value in the shear band in question (cf. [40]).

The experiments with dense samples revealed shear band widths of 7 ... 12 $d_{50,S1}$ for material *S1* and 14 ... 20 $d_{50,S2}$ for material *S2*. These values are in good agreement with above-mentioned 10 ... 20 d_{50}.
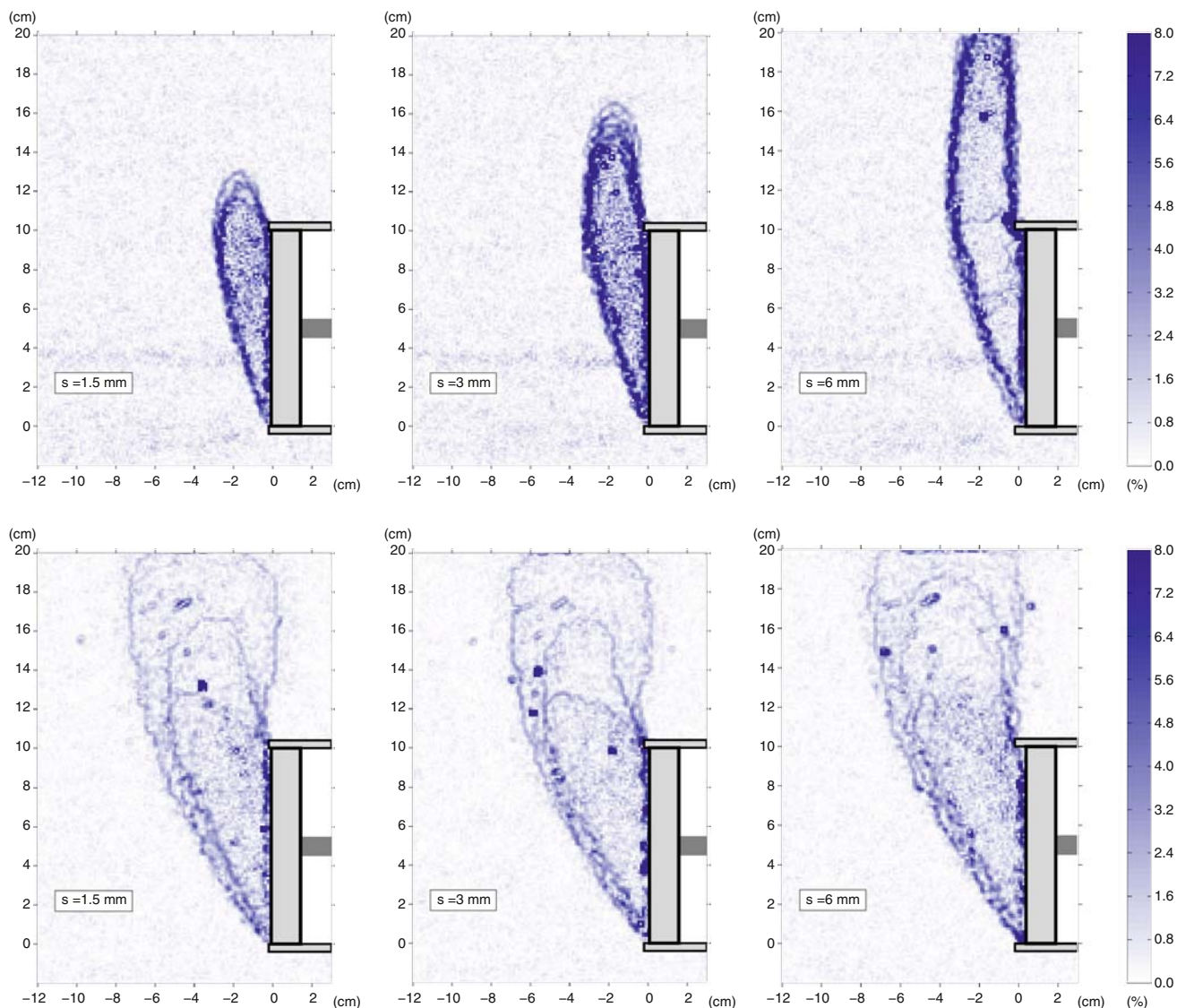
Fig. 10 Incremental shear strains I_2^ε for different advance steps and different relative densities in material *S1*; *top row*: dense sample ($I_d = 0.83$), *bottom row*: loose sample ($I_d = 0.26$). The single spots of "shear strain", especially in the pictures for the loose samples, are numerical artefacts due to outliers

2.6.4 Scaling effect

According to Stone and Muir Wood, "in order to maintain geometric similarity between the kinematic deformation mechanisms observed in models using sands with different particle sizes, the physical dimensions and boundary movements of the models should also be scaled in proportion to the particle size [49]". In the author's experiments, the dimensions of the model were not scaled, but it is possible to normalise the piston displacement, s, with the mean diameter of the sand particles d_{50}. Stone and Muir Wood mentioned that similar stages in the displacement pattern could be observed for $s/d_{50} = $ const.

Figure 13 shows the incremental shear strains for two dense samples of materials *S1* and *S2*. The extents of the

failure zones towards the soil surface, for a given s/d_{50}, were in fair agreement for both materials, also for *C/D* ratios other than 1.0. For the fine sand, the width of the chimney was considerably smaller, though.

The failure mechanism for material *S2* showed a noticeably larger inclination of the wedge, even though the respective friction angles were roughly equal (cf. Sect. 4). The reason for this different behaviour must be attributed to a scaling effect. Therefore, *quantitative* conclusions from model behaviour to prototype behaviour are hardly possible *for the dense samples*. But it is important to mention that the *qualitative* behaviour and general shape of the failure zone did not depend on grain size. Also, above restriction does not hold for the loose samples.
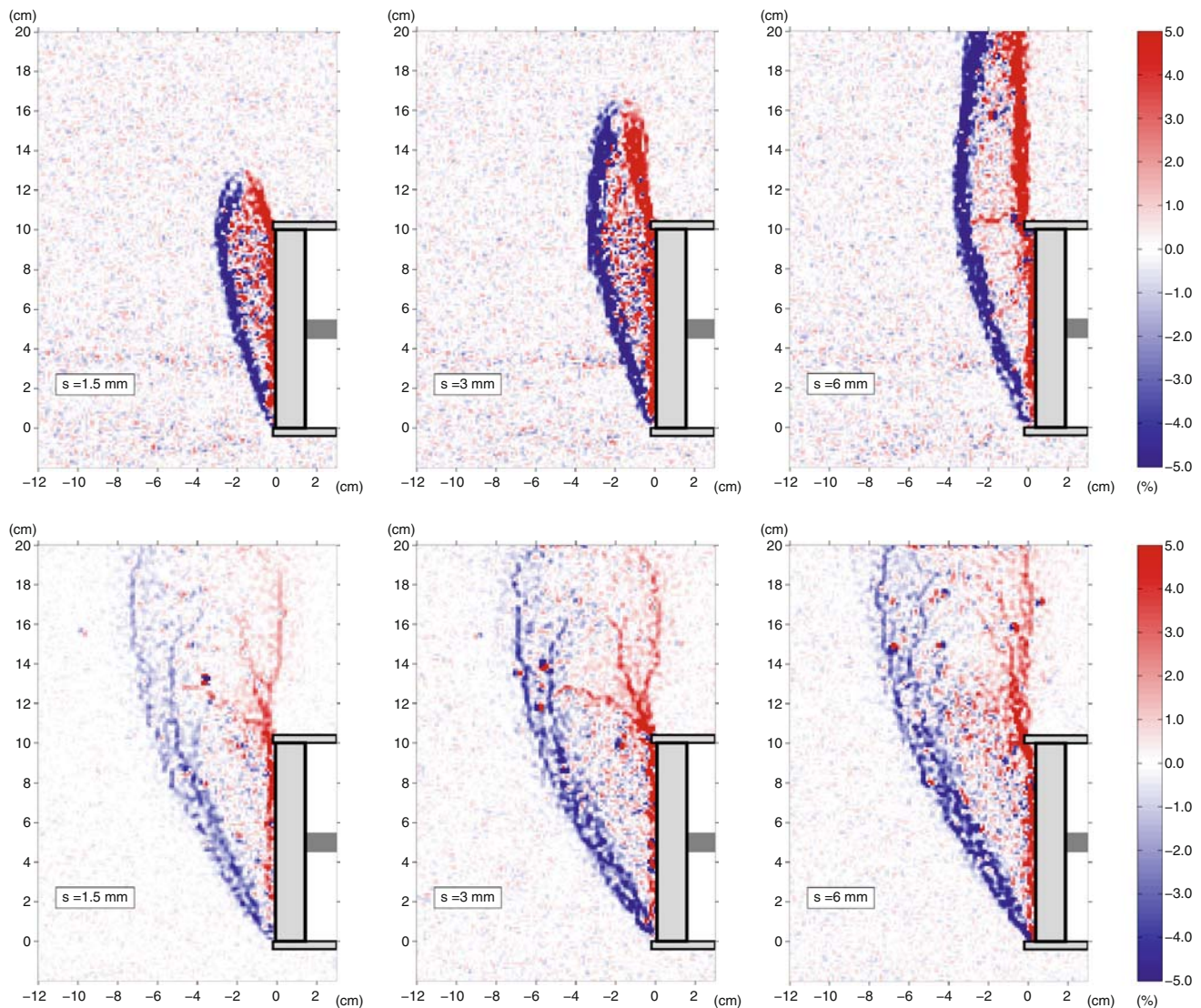
Fig. 11 Curl of the displacement field at different advance steps and different relative densities in material *S1*; top row: dense sample ($I_d = 0.83$), bottom row: loose sample ($I_d = 0.26$)

3 Investigation of the necessary support force

To validate the proposed models for the necessary support force/pressure, the model box was modified to allow for measurements of the resulting axial force on the piston.

3.1 Experimental set-up and tested materials

3.1.1 Sandbox and tunnel model

The model box for the second series of experiments is schematically sketched in Fig. 14, a picture of the box is displayed in Fig. 15. The tunnel was modelled with a hollow aluminium cylinder with an inner diameter of 10 cm and a wall thickness of 4 mm. As for the PIV measurements, the model tunnel protruded 7 cm into the

soil domain (Fig. 14 a). The distance between cylinder wall and bottom of the box was 5 cm. As a result of the PIV investigations, the dimensions of the box were considered large enough.

Wall friction was not considered to play a significant role and, therefore, no explicit investigation of wall friction on the side panels of the box was executed to evaluate its influence on the force measurements. This assumption is supported by Hauser [17], who published force measurements from small-scale model tests for coffer dams. With a comparable geometry, different configurations of wall friction (with and without teflon sheets between sand and side walls) did not show a significant influence on the measured force.

The face of the model tunnel was supported by an aluminium disc with a slightly smaller diameter than the inner
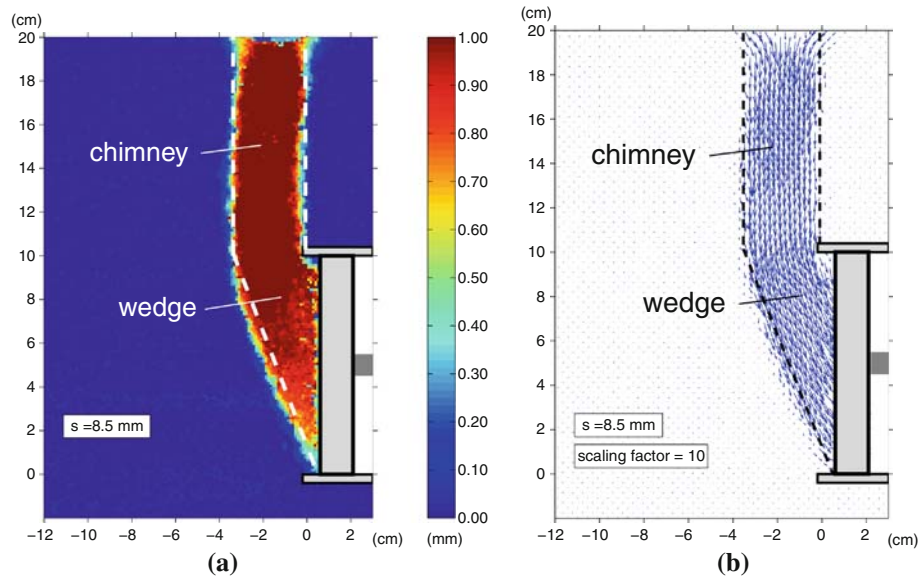
Fig. 12 Horn analogy of the failure zone for a piston advance step from 8.0 to 8.5 mm ($C/D = 1.0$; $I_d = 0.9$; S1). **a** Colour plot of incremental displacements. **b** Vector plot of incremental displacements
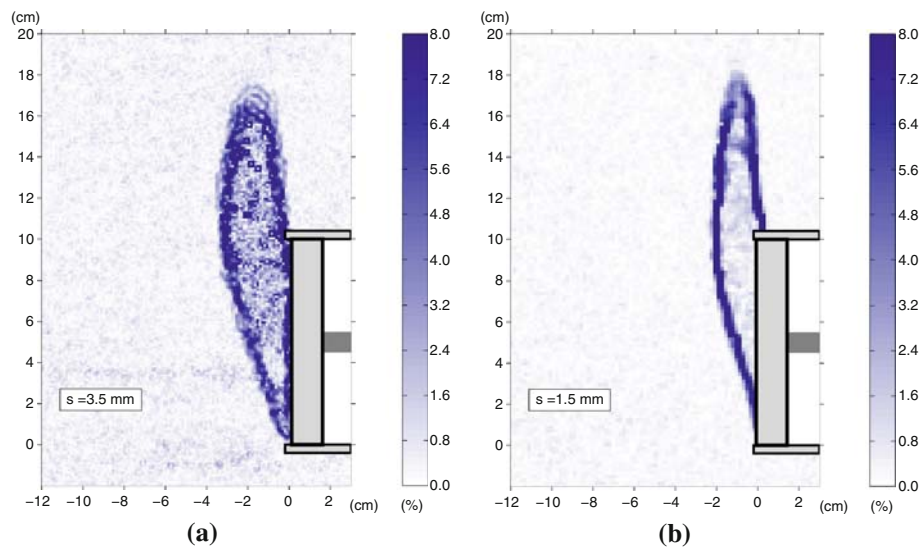

Fig. 13 Incremental shear strains for $C/D = 1.0$, dense samples. **a** material $S1$, $s/d_{50} = 3.5$ mm/0.58 mm ≈ 6.0. **b** material $S2$, $s/d_{50} = 1.5$ mm/ 0.24 mm ≈ 6.0

diameter of the tunnel ($D_{disc} = 9.8$ cm), thus eliminating friction between disc and tunnel. The piston rod was supported by a linear roller bearing, embedded in the side wall. The rod made contact with a miniature load cell that was mounted on a sliding carriage on the outside of the side wall. The carriage could be moved by turning a knob (Fig. 16).

3.1.2 Consideration of friction in the system

It was crucial to prevent any sand ingress into the gap between piston and model tunnel. This would have led to

an immediate obstruction of the piston, and thus stopped the experiment.

Therefore, piston and cylinder were covered with cling foil (Fig. 17). Talcum powder was applied between foil and piston.

3.1.3 Reference measurements with static water table

To quantify the friction within the whole system, reference measurements were made with hydrostatic water pressure. The idea of the reference measurements was to apply a *follower load*, i.e. a load that remained constant while
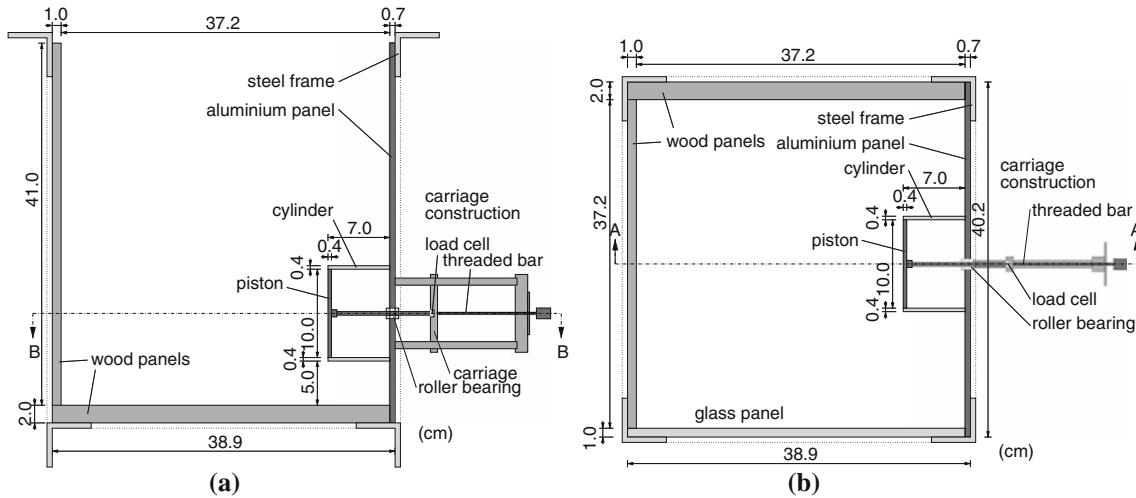
Fig. 14 Experimental set-up for the second set of experiments. **a** Longitudinal section A-A. **b** Plan section B-B
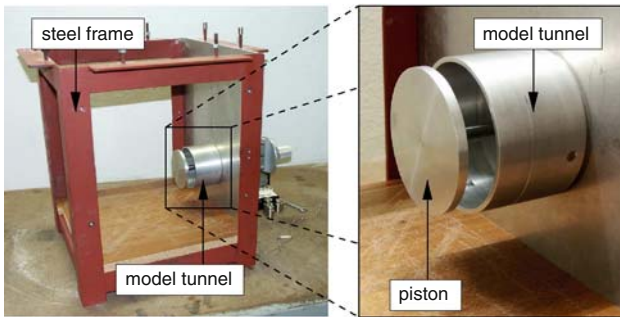

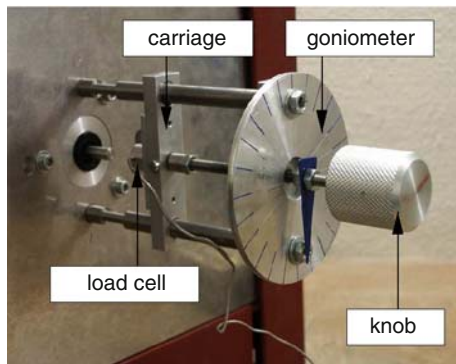**Fig. 15** Box and model tunnel for the second set of experiments

Fig. 16 Carriage construction with load cell, goniometer and turning knob

moving the piston. Thus, a difference between applied and measured force could be interpreted as overall friction.

The force acting on the piston was calculated to be:

$$F_{nom} = p_{w,centre} \cdot A_{piston}, \qquad (9)$$

with the water pressure $p_{w,centre}$ at the centre of the piston.

Two reference measurements with slightly different water tables at tunnel crown level were made. It became

Fig. 17 Model tunnel with cling foil protection against sand ingress

obvious that the force, registered by the load cell was lower than F_{nom}. The difference between F_{nom} and $F_{measured}$ was attributed to friction in the roller bearing and influence of the cling foil.

As a result, corrective terms ΔF_1 and ΔF_2 were derived, ΔF_2 as a function of piston advance s (cf. Fig. 18):

$$\Delta F_1(N) = 0.5 \qquad (10)$$

$$\Delta F_2(N) = 0.2 + 0.2\, s\,(mm). \qquad (11)$$

All measurements of the second test series, which are shown in the following, were corrected with ΔF_1 (full circles) *and* ΔF_2 (empty circles). The "true" load–displacement curves were expected in the range between $F_1 = F_{measured} + \Delta F_1$ and $F_2 = F_{measured} + \Delta F_2$.

3.2 Test procedure

3.2.1 Preparation of the sand body

In order to compare PIV evaluation and force measurements, the soil was prepared in the same way as described in Sect. 2.2
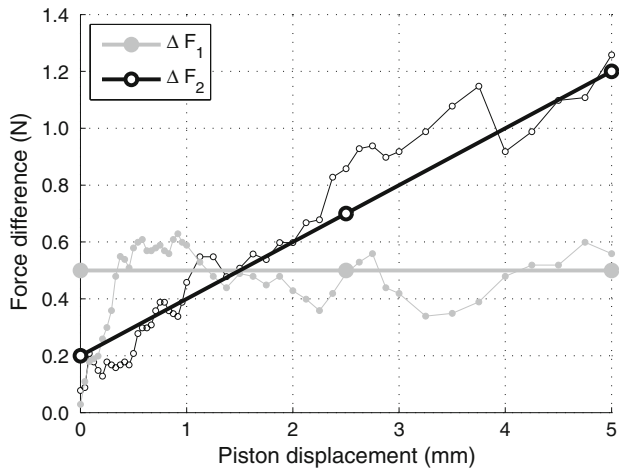
Fig. 18 Proposed correction functions for the force measurements

3.2.2 Steps of the model tests

The experiments were, again, performed displacement-controlled, by incrementally retracting the carriage. The piston rod was in contact with the carriage, and thus the load cell, which measured the resulting force exerted by the ground on the piston.

For the first millimetre of advance, displacement increments of $\Delta s = 0.042$ mm were applied. Thus, the force reduction for the very first displacements could be captured well. For $s > 1$ mm, the incremental advance was set to $\Delta s = 0.125$ mm.

For each combination of C/D and density I_d, at least two separate tests were performed to check the reproducibility of the results. An overall number of 52 tests were performed with $C/D = 0.25 \dots 2.0$ and (initially) dense and loose samples.

3.3 Results

3.3.1 Scaling effect and soil nonlinearity

As forces were measured in the second test series, the relations between force measurements on different scales had to be taken into consideration.

In analogy to the bearing capacity formula, the normalised support pressure *at failure* for cohesionless soil can be expressed as

$$N_D = \frac{p_f}{\gamma_d D}, \tag{12}$$

with the support pressure at failure p_f.

Necessary support pressures can be transferred from the model to the prototype scale, i.e. $(N_D)_{\text{model}} = (N_D)_{\text{prototype}}$, if the following relations are fulfilled:

$$\left(\frac{C}{D}\right)_{\text{model}} = \left(\frac{C}{D}\right)_{\text{prototype}}, \tag{13}$$

$$(I_d)_{\text{model}} = (I_d)_{\text{prototype}}, \tag{14}$$

$$(\varphi_c)_{\text{model}} = (\varphi_c)_{\text{prototype}}. \tag{15}$$

Especially, the determination of strength parameters on low stress levels is difficult. As will be outlined in Sect. 4, the critical state friction angle φ_c seems to be suited much better for the description of the problem than the peak friction angle $\varphi_p : \varphi_c$ can be considered independent of stress level and initial density; moreover, the observed load–displacement curves reach a sort of *critical state*, as will be shown in the following.

3.3.2 Evaluation method

In addition to uncertainties from the correction ΔF, the force readings showed a reasonable amount of scatter. To quantify the necessary support pressure N_D, all load–displacement curves were evaluated as shown in Fig. 19: an interval was defined manually, in which the force measurements reached a residual value. This interval was considered as range for the necessary support pressure N_D. The mentioned uncertainties only allow to quantify N_D as a range for each test.

In the following, the *mean values* for a correction with $\Delta F = (\Delta F_1 + \Delta F_2)/2$ serve to illustrate the general soil behaviour. For the sake of clarity, the bounds $F1$ and $F2$ are not plotted.

3.3.3 Load–displacement curves

The obtained load–displacement curves of loose and dense samples for a cover-to-diameter ratio $C/D = 1.0$ are shown in Fig. 20, which illustrates the difference between the
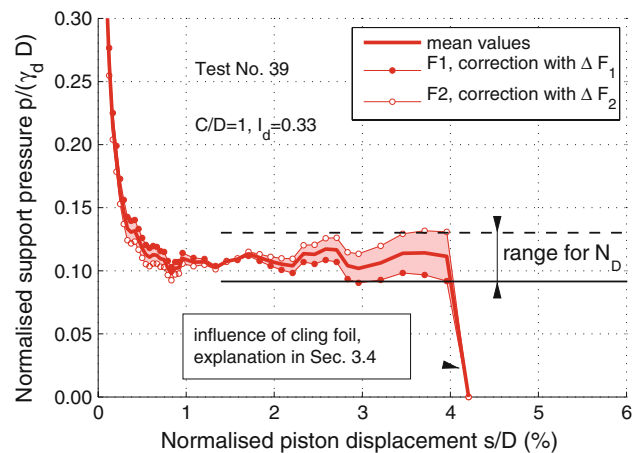

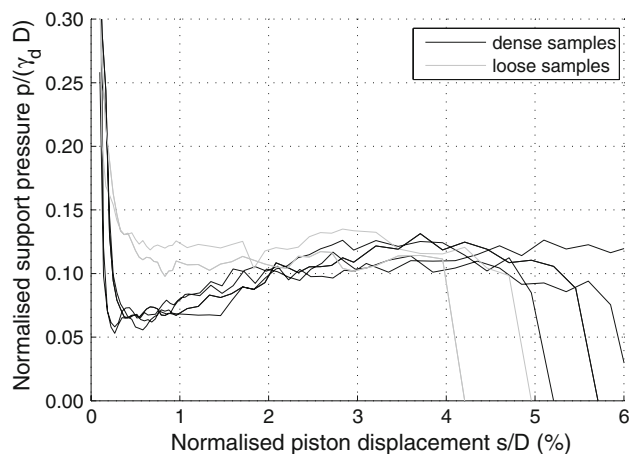**Fig. 19** Load–displacement curves for $C/D = 1.0$

Fig. 20 Development of normalised support pressure for $C/D = 1.0$, material $S1$

Fig. 21 Development of necessary support pressure for different C/D ratios

behaviour of loose and dense samples. The curves for dense sand dropped steeply to a relatively low value when compared with the curves for loose sand. But with continuing displacements, the resultant force on the piston in the dense samples increased again, reaching the same residual value for both curves after relative displacements of 2–3%.

The force readings dropped to zero after different advance steps for each test due to the influence of the cling foil. Otherwise, the tests were stopped at relative displacements of approx. 6 ... 7%.[1]

As illustrated in Fig. 21 for tests with material $S1$, the normalised support pressures for different overburdens arrived at the same residual value. In other words, the influence of C/D on the residual support pressure fell within the accuracy of the evaluation method.

3.4 Interpretation of results

The residual level of the normalised support pressure is interpreted as (dimensionless) necessary support pressure N_D: a lower pressure (in a pressure-controlled test or in the pressure chamber of a shield machine) would lead to infinite displacements, i.e. the collapse of the tunnel.

3.4.1 Influence of cling foil sealing

The influence of the cling foil becomes obvious as sharp pressure drop at the end of each test. The drop did not always occur at the same advance step, which leads to the conclusion that the drop was *not* due to friction in the apparatus, but depended on the cling foil configuration

---

[1] As protection measure for the load cell, the experiments for $C/D >$ 1.0 started with an initial displacement of 0.5 mm. Therefore, the curves seem shifted to the right.
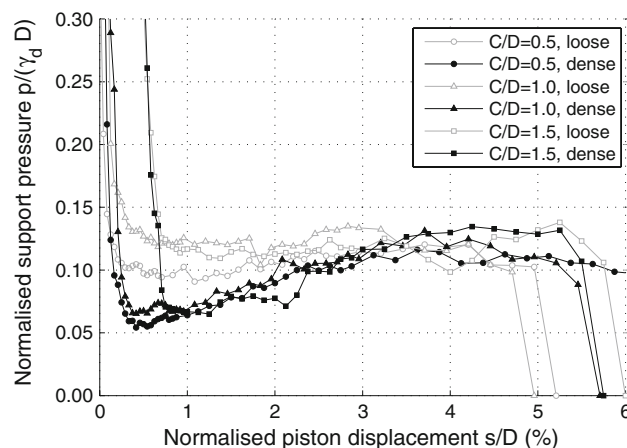
during preparation of the test. Moreover, the rising branch of force readings for nearly all dense samples suggests that the cling foil did not constrict the load transfer from soil to piston.

3.4.2 Influence of (relative) density

The generic shapes of the obtained load–displacement curves resemble the behaviour of sand in a shear test. After the peak in the stress–strain curve, the dense sand shows softening and loses strength. On the contrary, loose samples generally do not experience a peak, but reach their strength monotonically.

The behaviour of the dense samples in the experiments can be explained as follows:

- In the PIV analyses, a failure mechanism was detected that consists of a sliding wedge and an overlying chimney. For an advance step of $s/D = 2.0$ %, an arch can be observed. This arch redirects the weight above the sliding wedge onto the tunnel lining and the surrounding ground in such a way that the soil in front of the piston face builds up less pressure on the face.
- When the sliding wedge has formed, the shearing resistance of the sand influences the pressure on the tunnel face. As the shearing resistance of a dense sand decreases after the peak (*strain softening*), the force on the piston increases again.

The fact that "dense" and "loose" curves reach the same residual value (Fig. 22) suggests that the failure process is eventually governed by the critical state friction angle φ_c. A necessary support pressure $N_D(\varphi_c)$, which is determined using φ_c (rather than the peak friction angle φ_p) is always a safe estimate for a dense soil, also when large strains are reached. This interpretation overcomes some of the difficulties related to the transfer of results from model
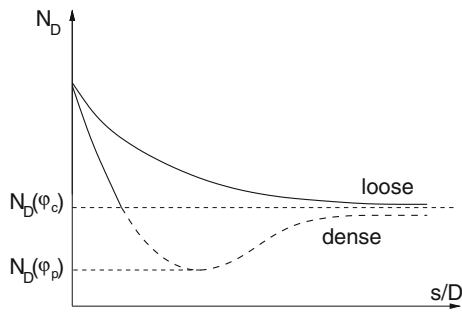
Fig. 22 Interpretation of "dense" and "loose" curves

Fig. 24 Development of necessary support pressure for different materials for $C/D = 1.0$

to prototype scale: conclusions from the model tests for *loose* sand (and *dense* sand at large strains) equally hold on the prototype scale, because φ_c can be considered independent of stress level.

Consideration of φ_p is only meaningful up to the peak strength; if larger strains cannot be ruled out, $N_D(\varphi_p)$ is unsafe.

3.4.3 Influence of overburden

Figure 23 summarises all results graphically. It shows the ranges for N_D for all 52 tests as bars. The bottom shows two plots of N_D vs. C/D, one for each material. The evaluation for material *S2* shows some scatter. Anyhow, there seems to be no influence of overburden on N_D, neither for *S1* nor *S2*. This is supported by experimental evidence by Léca and Dormieux [34] and numerical results by Ruse [43].

3.4.4 Influence of sand type

Figure 24 focusses on the influence of the sand type: it shows examples for the behaviour of materials *S1* and *S2* with comparable density in the sandbox tests. It can be concluded that, within the measurement accuracy, there is no significant influence of grain size distribution on the
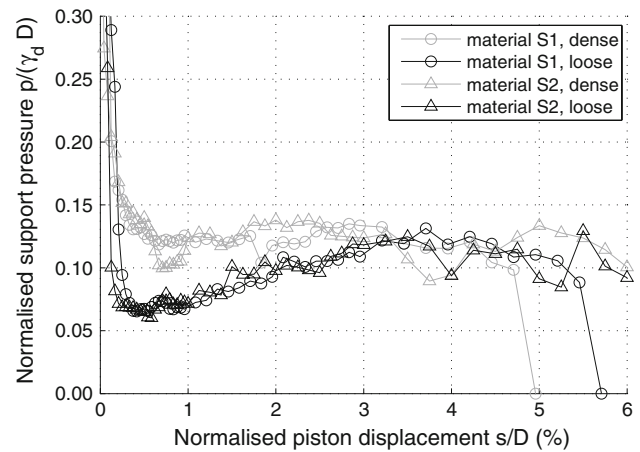
residual earth pressure on the piston. This observation is supported by an overview of all test results (Fig. 23), which indicates that the difference in N_D for both materials were marginal. In terms of necessary support pressure, the scaling effect is, therefore, smaller than the uncertainty of the evaluation method.

4 Critical evaluation of qualitative and quantitative results

4.1 Relation between qualitative and quantitative results

Both test series, the PIV investigation and the force measurements, were performed under the same conditions and with the same geometric configuration. Therefore, it is possible to relate results from both test series: Fig. 25 shows an example for incremental shear strains within the soil body at different stages throughout collapse of the face. As outlined earlier, the initially loose samples reveal
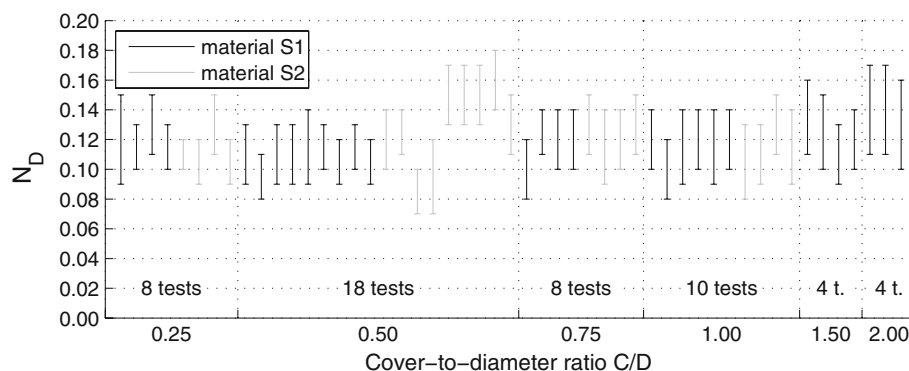

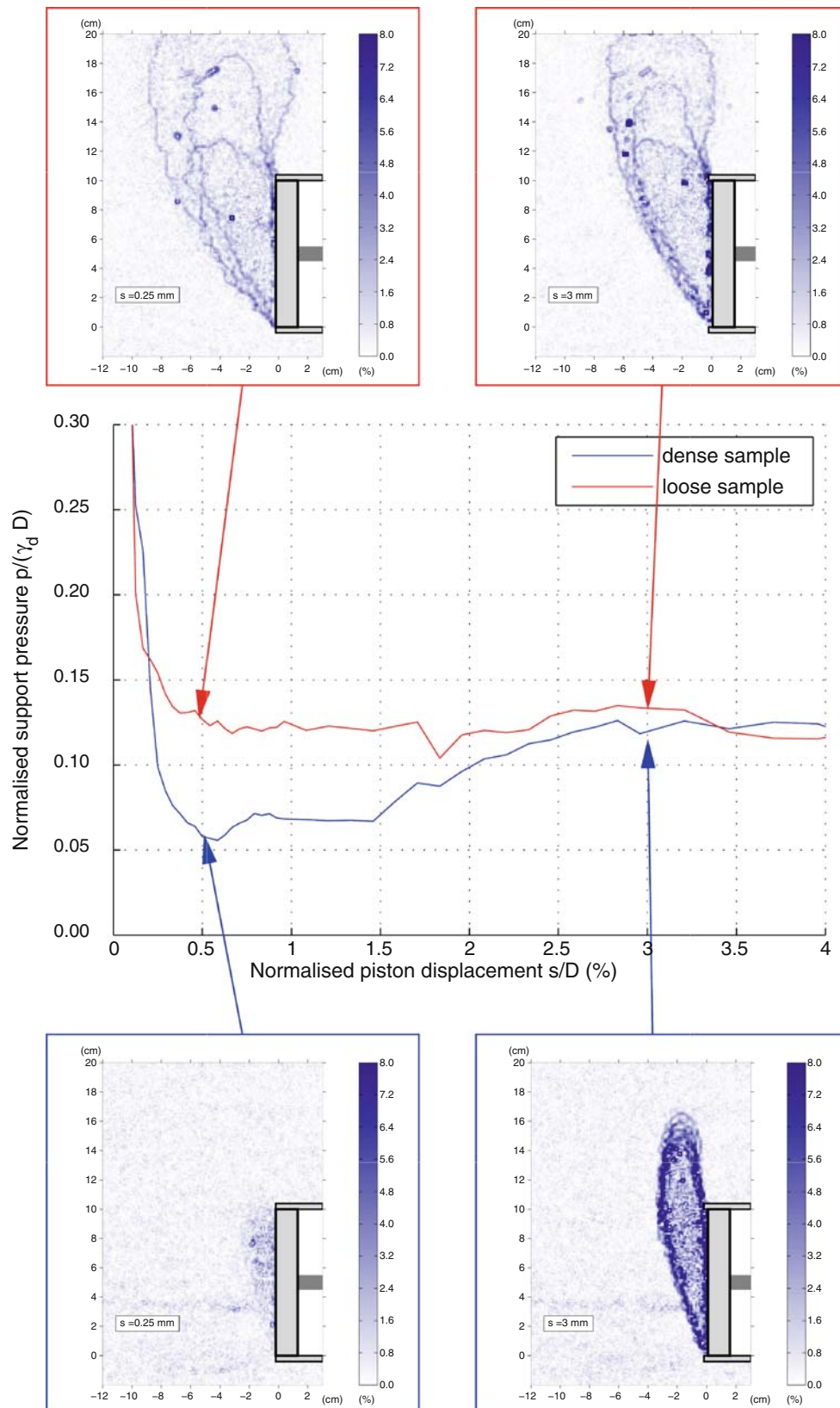**Fig. 23** Dependence of N_D on overburden ratio C/D

Fig. 25 Relation between incremental shear strain pattern and support pressure for material *S1*

the same pattern throughout the whole test. The dense samples, in contrast, show a development of the failure zone towards the ground surface.

At a point where the "dense" load–displacement curve has its minimum, only very small incremental shear strains are obtained. This supports the idea that the maximum strength of the soil is mobilised at this stage. After this minimum, the force on the piston rises again, and the failure zone develops towards the soil surface.

The failure mechanism has not yet reached the ground surface, when the load–displacement curve reaches its residual value. According to the silo equation, the vertical stresses reach a limit value once the silo has a height of roughly D_{silo}. From this point onwards, vertical load exerted by the chimney on the sliding wedge remains constant. This explains why the measured force does not increase any further.

It should be noted that, although the plots of incremental soil displacements shown in Sect. 2 reveal a completely different pattern for dense and loose samples, the residual N_D is identical. This holds evenly for the two applied sands $S1$ and $S2$.

4.2 Comparison with theoretical predictions

The results of the force measurements at low stress levels are compared with predictions of the various proposed models for an overburden $C/D = 1.0$. For this purpose, the strength parameters of the used material(s) must be known. As mentioned earlier, the author considers the critical state friction angle φ_c as governing strength parameter for the determination of a safe necessary support pressure N_D. In addition, the critical state friction angle φ_c is rather insensitive to size effects (cf. Sect. 2.1), which allows transfer of the small-scale results to the prototype scale.

The angle of repose of a loose tip of dry soil subjected to toe excavation serves as approximation to φ_c [6, 11]. Herle [19] suggested to slowly pour a pile of sand from a funnel and measure the slope of the pile. This method was used to investigate materials $S1$ and $S2$. An average angle of repose of $\varphi_{c,S1} = 32.5°$ (from $n = 44$ measurements, standard deviation $s_{\varphi c,S1} = 1.1°$) was obtained for material $S1$. For material $S2$, a value $\varphi_{c,S2} = 31.3°$ was obtained ($n = 20$, $s_{\varphi c,S2} = 1.4°$).

Figure 26 shows a comparison of theoretical predictions and experimental results in a plot of N_D vs. the critical friction angle φ_c. The comparison includes experimental data by Plekkenpol et al. [42] and Chambon and Corté [8], who quote friction angles in the order of 36°–42° for similar materials. Although not explicitly stated in the publications, the author understands that the quoted friction angles are *peak* friction angles. Both experimental campaigns provided a support pressure at the face of the model
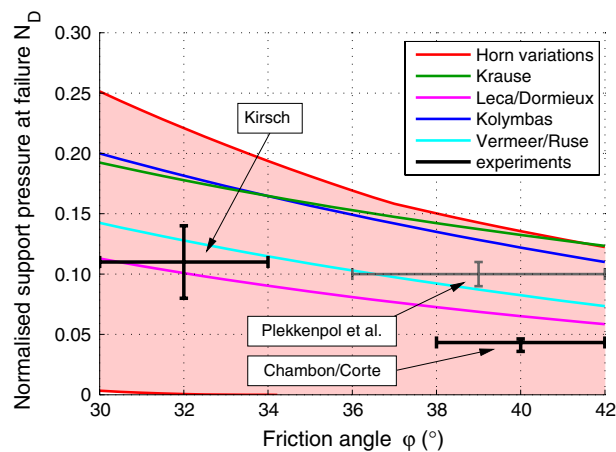

Fig. 26 Comparison of experimental results with theoretical predictions (the range of possible Horn predictions is shaded in *red* (resp. *light grey*))

tunnel that was gradually reduced. As the rising branch of the load–displacement curve for a dense sand (Fig. 22) cannot be captured in a stress-controlled test, the author believes that the quoted necessary support pressures N_D are valid for the peak strength, i.e. $N_D = N_D(\varphi_p)$.

The upper bound solution by Léca/Dormieux [34] and the empirical approach by Vermeer/Ruse [43] seem to approximate all experimental observations well.

5 Summary

For tunnels driven with slurry or EPB shields, the necessary support pressure in the excavation chamber must counteract water and earth pressure to prevent uncontrolled ground movements.

The author compiled a variety of theoretical, experimental and numerical approaches on the topic. A simple calculation with some representative approaches has shown that the predicted necessary support pressures can differ by as much as one order of magnitude.

To assess the quality of some proposed approaches, a tunnel face collapse was modelled with small-scale model tests at single gravity. Two test series served to investigate the evolution of the failure mechanism and the development of the necessary support force at the face in dry sand. In both series, the overburden above the model tunnel and the initial density of the soil were varied.

The investigation of failure mechanism was performed by means of Particle Image Velocimetry, which allowed to trace particle movements throughout a test. The resulting *displacement* patterns show that the overburden has a negligible influence on the extent and evolution of the failure zone. The latter is significantly influenced, though,

by the initial density of the sand: in dense sand a chimney-wedge-type collapse mechanism developed, which propagated towards the soil surface. Initially, loose sand did not show any development of a discrete collapse mechanism.

The support *force* was monitored during piston displacement. For displacements larger than 3% of the tunnel diameter, all curves reached approximately the same residual value, which was, in contrast to the failure zone, neither influenced by the overburden nor the initial density of the sand.

Analytical approaches from the literature were compared to the experimental results: the predictions by Ruse and Léca/ Dormieux showed a good agreement to the experimental results. The others overestimated the necessary support force.

References

1. Al Hallak R, Garnier J, Léca E (2000) Experimental study of the stability of a tunnel face reinforced by bolts. In: Kusakabe O, Fujita K, Miyazaki Y (eds) Geotechnical aspects of underground construction in soft ground. Balkema, Rotterdam, pp 65–68
2. Anagnostou G, Kovári K (1992) Ein Beitrag zur Statik der Ortsbrust beim Hydroschildvortrieb. In: Symposium '92, Probleme bei maschinellen Tunnelvortrieben? Gerätehersteller und Anwender berichten
3. Anagnostou G, Kovári K (1996) Face stability conditions with earth-pressure-balanced shields. Tunn Undergr Space Technol 11(2):165–173
4. Atkinson JH, Potts DM (1977) Stability of a shallow circular tunnel in cohesionless soil. Géotechnique 27(2):203–215
5. Balthaus H (1988) Standsicherheit der flüssigkeitsgestützten Ortsbrust bei schildvorgetriebenen Tunneln. In: Duddeck FH (ed) Institut für Statik der Technischen Universität Braunschweig. Springer, Berlin, pp 477–492
6. Bolton MD (1986) The strength and dilatancy of sands. Géotechnique 36(1):65–78
7. Bundesanstalt für Straßenwesen (BASt) (2007) ZTV-ING: Zusätzliche Technische Vertragsbedingungen und Richtlinien für Ingenieurbauten, Teil 5 Tunnelbau, Verkehrsblatt, Ausgabe 2003 und Entwurf 2007
8. Chambon P, Corté JF (1994) Shallow tunnels in cohesionless soil: stability of tunnel face. ASCE J Geotech Eng 120(7):1148–1165
9. Chambon P, Corté JF, Garnier J, König D (1991) Face stability of shallow tunnels in granular soils. In: Ko HY, McLean F (eds) Centrifuge 91. Balkema, Rotterdam, pp 99–105
10. Chambon P, Couillaud A, Munch P, Schürmann A., König D (1995) Stabilité du front de taille d'un tunnel: Étude de l'effet d'échelle, in Geo 95, p 3, cited in [54]
11. Cornforth DH (1973) Prediction of drained strength of sands from relative density measurements. In: Evaluation of relative density and its role in geotechnical projects involving cohesionless soils (in ASTM Spec. Techn. Publ. 523). American Society for Testing and Materials, Philadelphia, pp 281–303
12. DIN 18126 (1996) German Standard "Bestimmung der Dichte nichtbindiger Böden bei lockerster und dichtester Lagerung." Beuth, Berlin
13. Girmscheid G (2005) Tunnelbohrmaschinen - Vortriebsmethoden und Logistik, In: Betonkalender, Chap 1.3. Ernst & Sohn, Berlin, pp 119–256
14. Görtler H (1975) Dimensionsanalyse. Springer, Berlin
15. Graf B (1984) Theoretische und experimentelle Ermittlung des Vertikaldrucks auf eingebettete Bauwerke, No. 96 in Veröffentlichungen des Institutes für Bodenmechanik und Felsmechanik der Universität Karlsruhe
16. Gudehus G (2001) Grundbau Taschenbuch, Teil 1: Geotechnische Grundlagen. Chap Stoffgesetze für Böden aus physikalischer Sicht. Ernst & Sohn, Berlin
17. Hauser C (2005) Boden-Bauwerk-Interaktion bei parallel-wandigen Verbundsystemen, No. 29 in Berichte des Lehr- und Forschungsgebiets Geotechnik der Universität Wuppertal, Shaker, Aachen
18. Hejazi Y, Dias D, Kastner R (2008) Impact of constitutive models on the numerical analysis of underground constructions. Acta Geotech 3(4):251–258
19. Herle I (1997) Hypoplastizität und Granulometrie einfacher Korngerüste, No. 142 in Veröffentlichungen des Institutes für Bodenmechanik und Felsmechanik der Universität Karlsruhe
20. Höfle R, Fillibeck J, Vogt N (2008) Time dependent deformations during tunnelling and stability of tunnel faces in fine-grained soils under groundwater. Acta Geotech 3(4):309–316
21. Holzhäuser J. (2000) Problematik der Standsicherheit der Ortsbrust beim TBM-Vortrieb im Betriebszustand Druckluftstützung. In Beiträge anlässlich des 50. Geburtstages von Herrn Professor Dr.-Ing. Rolf Katzenbach, No. 52 in Mitteilungen des Institutes und der Versuchsanstalt für Geotechnik, Darmstadt University of Technology, pp 49–62
22. Holzhäuser J, Raleigh PC, Seeley TR (2004) Messtechnische Überwachung des Tunnelvortriebs mit 4 EPS-TBMs beim ECIS-Projekt in Los Angeles, in Seminar "Messen in der Geotechnik 2004", TU Braunschweig
23. Horn M (1961) Horizontaler Erddruck auf senkrechte Abschlussflächen von Tunneln. In: Landeskonferenz der ungarischen Tiefbauindustrie (German translation by STUVA, Düsseldorf)
24. Huang L, Xu Z, Zhou C (2009) Modeling and monitoring in a soft argillaceous shale tunnel. Acta Geotech 4(4):273–282
25. Kamata H, Mashimo H (2003) Centrifuge model test of tunnel face reinforcement by bolting. Tunn Undergr Space Technol 18:205–212
26. Kimura T, Mair RJ (1981) Centrifugal testing of model tunnels in soft soil. In: Proceedings of the 10th international conference on soil mechanics and foundation engineering, Stockholm, vol 1, pp 319–322
27. Kirsch A (2009) On the face stability of shallow tunnels in sand, No. 16 in Advances in Geotechnical Engineering and Tunnelling. Logos, Berlin
28. Kirsch A, Kolymbas D (2005) Theoretische Untersuchung zur Ortsbruststabilität. Bautechnik 82(7):449–456
29. Kolymbas D (2005) Tunnelling and tunnel mechanics. Springer, Berlin
30. Kolymbas D (2007) Geotechnik – Bodenmechanik, Grundbau und Tunnelbau, 2nd edn. Springer, Berlin
31. Krause T (1987) Schildvortrieb mit flüssigkeits- und erdgestützter Ortsbrust, No. 24 in Mitteilung des Instituts für Grundbau und Bodenmechanik der Technischen Universität Braunschweig
32. Labra C, Rojek J, Oñate E, Zarate F (2008) Advances in discrete element modelling of underground excavations. Acta Geotech 3(4):317–322
33. Laudahn A (2004) An approach to 1g modelling in geotechnical engineering with soiltron, No. 11 in Advances in Geotechnical Engineering and Tunnelling. Logos, Berlin

34. Leca E, Dormieux L (1990) Upper and lower bound solutions for the face stability of shallow circular tunnels in frictional material. Géotechnique 40(4):581–606

35. Mähr M (2005) Ground movements induced by shield tunnelling in non-cohesive soils, No. 14 in Advances in Geotechnical Engineering and Tunnelling. Logos, Berlin

36. Maranha J, Vieira A (2008) Influence of initial plastic anisotropy of overconsolidated clays on ground behaviour during tunnelling. Acta Geotech 3(3):259–271

37. Mayer PM, Hartwig U, Schwab C (2003) Standsicherheitsuntersuchungen der Ortsbrust mittels Bruchkörpermodell und FEM. Bautechnik 80:452–467

38. Mélix P (1987) Modellversuche und Berechnungen zur Standsicherheit oberflächennaher Tunnels, No. 103 in Veröffentlichungen des Institutes für Bodenmechanik und Felsmechanik der Universität Karlsruhe

39. Muir Wood D (2004) Geotechnical modelling. Spon, London

40. Nübel K (2002) Experimental and numerical investigation of shear localisation in granular material, No. 159 in Veröffentlichungen des Institutes für Bodenmechanik und Felsmechanik der Universität Karlsruhe

41. Nübel K, Weitbrecht V (2002) Visualization of localization in grain skeletons with particle image velocimetry. J Test Eval ASTM 30(4):322–329

42. Plekkenpol JW, van der Schrier JS, Hergarden HJ (2006) Shield tunnelling in saturated sand—face support pressure and soil deformations. In: Bezuijen A, van Lottum H (eds) Tunnelling: a decade of progress, GeoDelft 1995–2005. Taylor & Francis, London

43. Ruse NM (2004) Räumliche Betrachtung der Standsicherheit der Ortsbrust beim Tunnelvortrieb, No. 51 in Mitteilungen des Instituts für Geotechnik der Universität Stuttgart

44. Soubra AH (2000) Kinematical approach to the face stability analysis of shallow circular tunnels. In: 8th International symposium on plasticity, British Columbia, Canada, pp 443–445

45. Soubra AH (2000) Three-dimensional face stability analysis of shallow circular tunnels. In: International conference on geotechnical and geological engineering, Melbourne, Australia, November 19–24, pp 1–6

46. Soubra AH, Dias D, Emeriault F, Kastner R (2008) Three-dimensional face stability analysis of circular tunnels by a kinematical approach. In: GeoCongress 2008: characterization, monitoring, and modelling of GeoSystems (GSP 179). New Orleans, pp 894–901

47. Stallmann M (2005) Verbrüche im Tunnelbau – Ursachen und Sanierung. Diploma thesis, University of Applied Sciences Stuttgart

48. Sterpi D, Cividini A (2004) A physical and numerical investigation on the stability of shallow tunnels in strain softening media. Rock Mech Rock Eng 37(4):277–298

49. Stone KJL, Muir Wood D (1992) Effects of dilatancy and particle size observed in model tests on sand. Soils Found 32(4):43–57

50. STUVA (2001) Erarbeitung von Kriterien für den Einsatz von maschinellen Vortriebsverfahren im Tunnelbau, Auftraggeber Bundesanstalt für Straßenwesen (BASt), Tech. rep., (Studiengesellschaft für unterirdische Verkehrsanlagen e.V.)

51. Sveen J. (2004) An introduction to MatPIV 1.6.1. Eprint no. 2, ISSN 0809-4403, Department of Mathematics, Oslo University

52. Takano D, Otani J, Fukushige S, Natagani H (2006) Investigation of interaction behavior between soil and face bolts using X-ray CT. In: Desrues J, Viggiani G, Bèsuelle P (ed) Advances in X-ray tomography for geomaterials. ISTE Ltd., London, pp 389–395

53. Tatsuoka F, Goto S, Tanaka T, Tani K, Kimura Y (1997) Particle size effects on bearing capacity of footing on granular material. In: Asaoka A, Adachi T, Oka F (eds) Deformation and progressive failure in geomechanics. Pergamon, New York, pp 133–138

54. Technical Commitee 2 of ISSMGE – Physical Modelling in Geotechnics (2007) Catalogue of scaling laws and similitude questions in centrifuge modelling

55. Tejchman J (2004) FE-simulations of a direct wall shear box test. Soils Found 44(4):67–81

56. Tejchman J, Górski J (2007) FE-investigations of a deterministic and statistical size effect in granular bodies within a mico-polar hypoplasticity. Granul Matter 9:439–453

57. Vermeer PA, Ruse NM (2001) Die Stabilität der Tunnelortsbrust in homogenem Baugrund. Geotechnik 24(3):186–193

58. Vermeer PA, Ruse NM, Dong Z, Härle D (2000) Ortsbruststabilität von Tunnelbauwerken am Beispiel des Rennsteig-Tunnels. In: Tagungsband 2. TAE Kolloquium, Bauen in Boden und Fels, pp 195–202

59. Vermeer PA, Ruse NM, Marcher T (2002) Tunnel heading stability in drained ground. Felsbau 20(6):8–18

60. Walz B (2006) Der 1g-Modellversuch in der Bodenmechanik – Verfahren und Anwendung, No. 40 in Veröffentlichungen des Grundbauinstitutes der Technischen Universität Berlin, Vorträge zum 2. Hans Lorenz Symposium

61. Walz B (2006) Möglichkeiten und Grenzen bodenmechanischer 1g-Modellversuche. In: Rackwitz F (ed) Entwicklungen in der Bodenmechanik, Bodendynamik und Geotechnik. Springer, Berlin, pp 63–78

62. White DJ, Take WA, Bolton MD (2001) A deformation measurement system for geotechnical testing based on digital imaging, close-range photogrammetry, and PIV image analysis. In: Proceedings of the 15th international conference on soil mechanics and foundation engineering, Istanbul. Balkema, Rotterdam, pp 539–542

63. White DJ, Take WA, Bolton MD (2001) Measuring soil deformation in geotechnical models using digital images and PIV analysis. In: Proceedings of the 10th international conference on computer methods and advances in geomechanics, Tucson, Arizona. Balkema, Rotterdam, pp 997–1002